Palacios, L., Ceriotti, M. and Radice, G. (2015) Close proximity formation flying via linear quadratic tracking controller and artificial potential function. *Advances in Space Research*, 56(10), pp. 2167-2176. (doi:10.1016/j.asr.2015.09.005)

This is the author's final accepted version.

There may be differences between this version and the published version. You are advised to consult the publisher's version if you wish to cite from it.

http://eprints.gla.ac.uk/109736/

Deposited on: 27 March 2017

Close Proximity Formation Flying via Linear Quadratic Tracking Controller and Artificial Potential Function

Leonel Palacios[1], Matteo Ceriotti and Gianmarco Radice
University of Glasgow, Glasgow, Scotland, G12 8QQ, United Kingdom

Abstract

A Riccati-based tracking controller with collision avoidance capabilities is presented for proximity operations of spacecraft formation flying near elliptic reference orbits. The proposed dynamical model incorporates nonlinear accelerations from an artificial potential field, in order to perform evasive maneuvers during proximity operations. In order to validate the design of the controller, test cases based on the physical and orbital features of the Prototype Research Instruments and Space Mission Technology Advancement (PRISMA) will be implemented, extending it to scenarios with multiple spacecraft performing reconfigurations and on-orbit position switching. The results show that the tracking controller is effective, even when nonlinear repelling accelerations are present in the dynamics to avoid collisions, and that the potential-based collision avoidance scheme is convenient for reducing collision threat.

Keywords: Artificial Potential Functions, Autonomous Control, Collision Avoidance, Formation Flying, Tracking Control

1. Introduction

The idea of autonomous spacecraft flying in tight formation, with maximum separation baselines of a few hundred meters, especially in low Earth orbits (LEOs), has generated widespread interest over the last several years. The constantly evolving notion of spacecraft formation provides the means to enhance mission reliability and adaptability to changing mission requirements by distributing major tasks, which used to be commonly handled by a single monolithic unit, among several smaller spacecraft, therefore leading to technological and economic benefits such as: mission robustness against unit loss by reconfiguring the formation with the remaining satellites, weight reduction in launch payload for tight formation missions, miniaturization and mass production of spacecraft, etc. Moreover, autonomy poses several advantages over traditional manual control, such as the reduction of ground-based orbit maintenance, planning and scheduling by knowing the future position and velocity of the spacecraft at any time and lower propellant usage by continuously maintaining the orbit at its highest level (De Florio et al., 2014). Several autonomous formation flying missions designed to demonstrate the feasibility of this technology are currently deployed while others are still under development, for example, TacSat2 (Plam et al., 2008), Demeter (Lamy et al., 2009), TanDEM-X (Montenbruck & Kahle, 2008) and PRISMA (D'Amico et al., 2013).

Nevertheless, autonomous formation flying presents difficult control challenges which rise in complexity as the number of elements in the formation increases or when proximity operations are required. Having a large number of spacecraft in close formation requires to execute complex maneuvers with minimal fuel consumption and reliable collision avoidance systems. To account for these tasks, several control strategies have been studied; the Linear Quadratic Regulator (LQR) applied to the control of spacecraft in formation using the Clohessy-Wiltshire (CW) (Clohessy & Wiltshire, 1960) model for circular reference orbits, was used by Starin (Starin, 2001) where an infinite time cost function was minimized by the algebraic Riccati equation. Bainum et al. (Bainum et al., 2005) presented further studies where the LQR was used along with the Tschauner and Hempel (TH) (Tschauner & Hempel, 1965) model for elliptic reference orbits. Capo-Lugo and Bainum (Capo-Lugo & Bainum, 2007) used the LQR and the TH model to maintain the separation distance between a pair of satellites for the

---

[1] *Email address:* l.palacios-moreno.1@research.gla.ac.uk

NASA Benchmark Tetrahedron Constellation. This was accomplished while providing minimum time and fuel consumption through two different approaches, adapting the time-varying term in the TH equations in a piecewise manner and using the TH equations as a time-varying dynamical system. Yoo et al. (Yoo et al., 2013) presented fuel balancing strategies for maneuvers between projected circular orbits, subject to the CW dynamics, formulating the optimal control problem from Palmer's CW analytical solution for general configurations (Palmer, 2006). Moreover, Huang et al. (Huang et al., 2014) used controlled Lorentz forces on an electrostatically charged spacecraft as propellant less electromagnetic propulsion for orbital maneuvering in the planetary magnetic field. For this purpose, a closed-loop integral sliding mode controller was designed to effectively track a trajectory when external disturbances are also present. Artificial potential fields (APF) have been also applied to the control of spacecraft in formation by strongly relying on the theory of dynamical systems. Bennet and McInnes (Bennet & McInnes, 2008) implemented a control scheme based on attractive/repulsive APF grounded in the theory of bifurcation to command the formation keeping of spacecraft and the transition during maneuvering, providing a wide variety of configurations with only a single parameter change. Badawy and McInnes (Badawy & McInnes, 2008) used the concept of superquadric potential fields, which allows the accurate modelling of the geometry of any orbital element, for on-orbit assembly of large space structures. McCamish et al. (McCamish et al., 2007) have also investigated mixed control strategies, such as APF and LQR, to perform rendezvous and assembly maneuvers using the CW relative dynamics near a circular orbit. In nonlinear control with APF, Lee et al. (Lee et al., 2015) developed a decentralized, six-degree-of-freedom tracking control scheme using Lie group theory and a Lennard-Jones potential. The simulated scenarios use a virtual leader approach and focus on formation keeping using highly elliptical reference orbits, leading to almost global asymptotic convergence to the desired trajectory.

The objective of this paper is to present the design of a mixed LQR/APF tracking controller for close-maneuvering spacecraft in formation using dynamics of relative motion linearized near an elliptical reference orbit. Contrasted with other LQR/APF formulations, the proposed control strategy has the capacity to deal with both circular and elliptical reference orbits, providing guidance and tracking toward target nominal trajectories while optimizing fuel consumption by Riccati procedure; additionally, the collision avoidance scheme, generated from a Gaussian-like potential function, is defined in terms of both spacecraft and obstacle position and velocity, ensuring evasive actions between the elements of the formation using repelling accelerations. This paper starts presenting first the equations of relative motion to be used, including its state-space representation and energy matching conditions for local bounded relative motion in Section 2. The controller is then presented in Section 3, where the collision avoidance guidance scheme is developed. Next, in Section 4, the selected test cases and results are introduced using elliptical reference orbits. Finally, conclusions are found in Section 5.

2. Linear Equations of Relative Motion

Consider two spacecraft orbiting around the Earth. One of the spacecraft is called leader and the other the follower. Let r and θ denote the radius and the true anomaly of the reference orbit of the leader spacecraft, respectively. In the Local Vertical Local Horizontal (LVLH) reference frame, the linear equations of the relative dynamics of the follower with respect to the leader, in component-wise manner, can be represented as (Inalhan et al., 2002)

$$\ddot{x} - 2\dot{\theta}\dot{y} - \ddot{\theta}y - \dot{\theta}^2 x = 2n^2 \left(\frac{1 + e\cos\theta}{1 - e^2} \right)^3 x$$

$$\ddot{y} + 2\dot{\theta}\dot{x} + \ddot{\theta}x - \dot{\theta}^2 y = -n^2 \left(\frac{1 + e\cos\theta}{1 - e^2} \right)^3 y \qquad (1)$$

$$\ddot{z} = -n^2 \left(\frac{1 + e\cos\theta}{1 - e^2} \right)^3 z$$

with n being the mean motion and e the eccentricity of the reference orbit. A tracking dynamical system, capable of following a nominal trajectory, can be designed in matrix representation using Eq. (1), adding a control input $\boldsymbol{u} \in \mathbb{R}^3$ and a nonlinear term $\mathbf{N} \in \mathbb{R}^6$ to account for external perturbations. With the definition of the tracking vector between the current state $\boldsymbol{x} = \begin{bmatrix} x & y & z & \dot{x} & \dot{y} & \dot{z} \end{bmatrix}^{\mathrm{T}}$ and the nominal state $\boldsymbol{x}_n = \begin{bmatrix} x_n & y_n & z_n & \dot{x}_n & \dot{y}_n & \dot{z}_n \end{bmatrix}^{\mathrm{T}}$ as $\delta\boldsymbol{x} = \boldsymbol{x} - \boldsymbol{x}_n \in \mathbb{R}^6$, the tracking dynamics can be represented as

$$\delta \dot{x}(t) = \mathbf{A}(t)\delta x(t) + \mathbf{B}(t)\delta u(t) + \delta \mathbf{N} \tag{2}$$

where $\delta u = u - u_n$ and $\delta \mathbf{N} = \mathbf{N} - \mathbf{N}_n$. The dynamics matrix $\mathbf{A} \in \mathbb{R}^{6 \times 6}$ and the control matrix $\mathbf{B} \in \mathbb{R}^{6 \times 3}$ are defined as follows (Bate et al., 1971)

$$\mathbf{A}(t) = \begin{bmatrix} \mathbf{0}_3 & \mathbf{I}_3 \\ \tilde{\mathbf{A}} & \bar{\mathbf{A}} \end{bmatrix} \qquad \mathbf{B} = \begin{bmatrix} \mathbf{0}_3 \\ \mathbf{I}_3 \end{bmatrix}$$

$$\bar{\mathbf{A}} = \begin{bmatrix} 0 & 2\dot{\theta} & 0 \\ -2\dot{\theta} & 0 & 0 \\ 0 & 0 & 0 \end{bmatrix} \qquad \tilde{\mathbf{A}} = \begin{bmatrix} a_{41} & \ddot{\theta} & 0 \\ -\ddot{\theta} & a_{52} & 0 \\ 0 & 0 & a_{63} \end{bmatrix} \tag{3}$$

Here $\mathbf{0}_3 \in \mathbb{R}^{3 \times 3}$, $\mathbf{I}_3 \in \mathbb{R}^{3 \times 3}$ and the matrix elements are given as

$$a_{41} = \dot{\theta}^2 + 2n^2 \left(\frac{1 + e\cos\theta}{1 - e^2} \right)^3$$

$$a_{52} = \dot{\theta}^2 - n^2 \left(\frac{1 + e\cos\theta}{1 - e^2} \right)^3$$

$$a_{63} = -n^2 \left(\frac{1 + e\cos\theta}{1 - e^2} \right)^3 \tag{4}$$

$$\dot{\theta} = \frac{n}{\left(1 - e^2\right)^{3/2}} \left(e^2 \cos^2\theta + 2e\cos\theta + 1 \right)$$

$$\ddot{\theta} = -\frac{2en\sin\theta\,\dot{\theta}}{\left(1 - e^2\right)^{3/2}} \left(e\cos\theta + 1 \right)$$

where θ can be obtained from Kepler's equation. Introducing appropriate initial conditions to Eq. (1) allows the follower to orbit bounded paths around the center of the formation without any control effort, when disturbances are not acting on it. In order to exhibit periodicity in the relative motion (locally bounded relative motion), period commensurability must exist between the absolute orbit of the follower and the leader. Since the semi-major axis of an elliptic orbit determines its energy, it is possible to use energy matching conditions (EMC), together with the initial state of the follower, to find bounded relative motion by equating the orbit energy of the leader and the follower (Gurfil, 2005). If ε and a are the energy and the semimajor axis of an elliptic orbit, respectively, then

$$\varepsilon_{leader} = \varepsilon_{follower}$$
$$-\frac{\mu}{2a} = \frac{1}{2}\left(\dot{x}_0 - \dot{\theta}_0 y_0 + \dot{r}_0\right)^2 + \left[\dot{y}_0 + \dot{\theta}_0\left(x_0 + r_0\right)\right]^2 + \dot{z}^2 - \frac{\mu}{\sqrt{\left(r_0 + x_0\right)^2 + y_0^2 + z_0^2}} \tag{5}$$

where the subscript 0 indicates an initial condition.

3. Control Strategy Design

The procedure to control formation maneuvers consists of two parts: tracking and collision avoidance. First, the tracking of the nominal trajectories x_n is achieved through the linear quadratic regulator (LQR) to minimize a quadratic cost function

$$\mathcal{J} = \frac{1}{2}\left[x(t_f) - x_n(t_f)\right]^T \mathbf{F}(t_f)\left[x(t_f) - x_n(t_f)\right]$$
$$+ \frac{1}{2}\int_{t_0}^{t_f} \left\{\left[x(t) - x_n(t)\right]^T \mathbf{Q}(t)\left[x(t) - x_n(t)\right] + \left[u(t) - u_n(t)\right]^T \mathbf{R}(t)\left[u(t) - u_n(t)\right]\right\} dt \tag{6}$$

subject to the relative dynamics of Eq. (2) with the weight matrices $\mathbf{F}(t) \geq \mathbf{0} \in \mathbb{R}^{6\times 6}$, $\mathbf{Q}(t) \geq \mathbf{0} \in \mathbb{R}^{6\times 6}$ and $\mathbf{R}(t) > \mathbf{0} \in \mathbb{R}^{3\times 3}$. To provide an optimal solution to this problem a Riccati procedure, also called the sweep method, is used along the control law of the form (Bryson & Ho, 1975)

$$\delta\boldsymbol{u}(t) = \mathbf{K}(t)\delta\boldsymbol{x}(t) \tag{7}$$

where the Kalman gain $\mathbf{K}(t)$ is defined as $\mathbf{K}(t) = \mathbf{R}^{-1}(t)\mathbf{B}^{\mathrm{T}}(t)\mathbf{P}(t)$ and $\mathbf{P}(t) \in \mathbb{R}^{6\times 6}$ is the solution of the Matrix Riccati Equation (MRE)

$$\dot{\mathbf{P}}(t) = -\mathbf{P}(t)\mathbf{A}(t) - \mathbf{A}^{\mathrm{T}}(t)\mathbf{P}(t) + \mathbf{P}(t)\mathbf{B}(t)\mathbf{R}^{-1}(t)\mathbf{B}^{\mathrm{T}}(t)\mathbf{P}(t) - \mathbf{Q}(t) \quad \text{with } \mathbf{P}(t_f) = \mathbf{F}(t_f) \tag{8}$$

It is worth mentioning that Eq. (8) does not depend on the state initial conditions nor the desired output; it can be computed offline.

Collision avoidance during maneuvering is achieved through repulsive accelerations created by artificial potential functions (APFs) (McInnes, 1993). The accelerations, obtained through the negative gradient of the APF, result in a non-linear continuous dynamical system in which stability can be investigated robustly and mathematically by Lyapunov methods. The main feature of this scheme is that it accounts for the separation distance and velocity of both spacecraft and obstacles without the previous knowledge of their trajectories (Ge & Cui, 2002). To obtain such accelerations, the proposed potential function U is defined as a Gaussian-like function

$$U = \mathrm{A}_m \exp\left[-\frac{9(d-d_a)^2}{2D^2}\right] \tag{9}$$

where the element A_m is a positive scaling constant defined as (McQuade & McInnes, 1997)

$$\mathrm{A}_m = \frac{\lambda\left(D + \|\boldsymbol{x}_o\| - \|\boldsymbol{x}_n\|\right)}{6\exp(-3D)} \tag{10}$$

Here λ is a scaling factor for the strength of the potential, $\boldsymbol{\rho}$ is the relative position of the spacecraft and D is a positive constant that determines the influence range of the potential. The scalar variables d and d_a are defined as follows. It is assumed that the relative position and velocity of an obstacle $\boldsymbol{x}_o = [\boldsymbol{\rho}_o \quad \boldsymbol{v}_o]^{\mathrm{T}}$ are currently known. The component of the relative velocity between the spacecraft and the obstacle in the direction of the obstacle is defined as

$$v_{so\|} = [\boldsymbol{v} - \boldsymbol{v}_o]^{\mathrm{T}} \cdot \hat{\boldsymbol{n}}_\| \tag{11}$$

where $\hat{\boldsymbol{n}}_\|$ is a unit vector directed from the spacecraft to obstacle and is defined as

$$\hat{\boldsymbol{n}}_\| = \frac{\boldsymbol{\rho}_o - \boldsymbol{\rho}}{\|\boldsymbol{\rho}_o - \boldsymbol{\rho}\|} \tag{12}$$

The symbol $\| \quad \|$ represents Euclidean norm defined as $\|\boldsymbol{\alpha}\|_2 = \left[\alpha_1^2 + \alpha_2^2 + \cdots \alpha_j^2\right]^{1/2} \in \mathbb{R}^j$. In Eq. (12), the quantity $d = \|\boldsymbol{\rho}_o - \boldsymbol{\rho}\|$ represents the separation distance between spacecraft and obstacle. If $v_{so\|} \leq 0$, then the spacecraft is moving away from the obstacle, and in principle there is no need to implement evasive maneuvers. On the other hand, if $v_{so\|} > 0$, then it is required to reduce this velocity to zero within a distance d_a, which can be achieved by selecting a deceleration value a_d and using the following expression:

$$d_a = \frac{v_{so\|}^2}{2a_d} \tag{13}$$

The potential U can be implemented by tuning its parameters depending on the problem requirements. For example, Fig. 1 shows a plot of the surface and the associated contours of the potential in Eq. (9) where D represents the extension of the potential and λ its gradient.
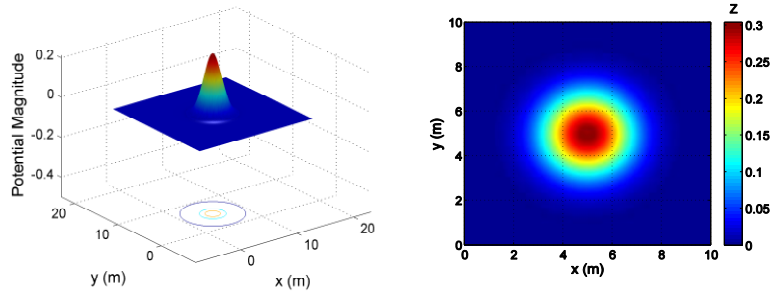
a) $\lambda = 3 \times 10^{-8}$ and $D = 10$ m
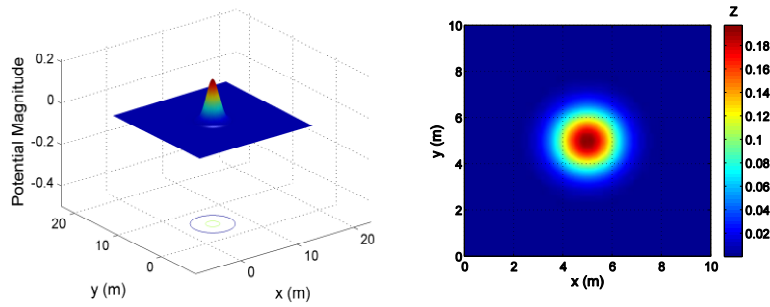
b) $\lambda = 3 \times 10^{-7}$ and $D = 5$ m

Fig. 1: Potential distribution

Moreover, the corresponding repulsive acceleration can be defined as the negative gradient of the potential with respect to the spacecraft position and velocity and denoted by

$$\mathbf{N}(\boldsymbol{x}, \boldsymbol{x}_o) = -(\nabla_{\boldsymbol{\rho}} U + \nabla_v U) \tag{14}$$

Next, Eq. (14) is evaluated to result in the following expression

$$\mathbf{N}(\boldsymbol{x}, \boldsymbol{x}_o) = \frac{9 \mathrm{A}_m (d - d_a)}{D^2} \exp\left[-\frac{9(d - d_a)^2}{2D^2} \right] \left(\frac{\partial}{\partial \boldsymbol{\rho}} + \frac{\partial}{\partial v} \right) (d - d_a) \tag{15}$$

with its corresponding derivatives

$$
\begin{aligned}
\frac{\partial}{\partial \boldsymbol{\rho}} d &= -\hat{\boldsymbol{n}}_{\parallel} \\
-\frac{\partial}{\partial \boldsymbol{\rho}} d_a &= -\frac{v_{so\parallel}}{a_d} \left\{ \frac{1}{d} \left[\boldsymbol{v}_{so\parallel} - (\boldsymbol{v} - \boldsymbol{v}_o) \right] \right\} \\
\frac{\partial}{\partial v} d &= 0 \\
-\frac{\partial}{\partial v} d_a &= -\frac{v_{so\parallel}}{a_d} \hat{\boldsymbol{n}}_{\parallel}
\end{aligned}
\tag{16}
$$

In order to help to visualize the nature of the evasive movement, the acceleration $\mathbf{N}(\boldsymbol{x}, \boldsymbol{x}_o)$ can be defined in terms of the velocity component $v_{so\perp}$ in the direction of the unit vector $\hat{\boldsymbol{n}}_{\perp}$ normal to $\hat{\boldsymbol{n}}_{\parallel}$, as observed in Fig. 2, where

$$v_{so\perp} = \sqrt{\|\boldsymbol{v} - \boldsymbol{v}_o\|^2 - v_{so\|}^2}$$

$$\hat{\boldsymbol{n}}_\perp = \frac{(\boldsymbol{v} - \boldsymbol{v}_o) - v_{so\|}\hat{\boldsymbol{n}}_\|}{\|(\boldsymbol{v} - \boldsymbol{v}_o) - v_{so\|}\hat{\boldsymbol{n}}_\|\|}$$

(17)

Then, using the relationship $\boldsymbol{v}_{so\perp} = (\boldsymbol{v} - \boldsymbol{v}_o) - \boldsymbol{v}_{so\|}$ leads the second equation in the set of Eq. (16) to become $-\dfrac{\partial}{\partial \boldsymbol{\rho}} d_a = \dfrac{v_{so\|}}{a_d} \dfrac{1}{d} v_{so\perp} \hat{\boldsymbol{n}}_\perp$. The final expression of the repulsive acceleration is given by

$$\mathbf{N}(\boldsymbol{x}, \boldsymbol{x}_o) = \frac{9\mathrm{A}_m(d - d_a)}{D^2} \exp\left[-\frac{9(d - d_a)^2}{2D^2} \right] \left[-\left(1 + \frac{v_{so\|}}{a_d} \right) \hat{\boldsymbol{n}}_\| + \frac{v_{so\|}v_{so\perp}}{da_d} \hat{\boldsymbol{n}}_\perp \right]$$

(18)

In Eq. (18), two different components can be observed; the first, in the opposite direction of $\hat{\boldsymbol{n}}_\|$, is used to repel the spacecraft from the obstacle; the second, in the direction of $\hat{\boldsymbol{n}}_\perp$, is used to steer the spacecraft during the evasive maneuver.
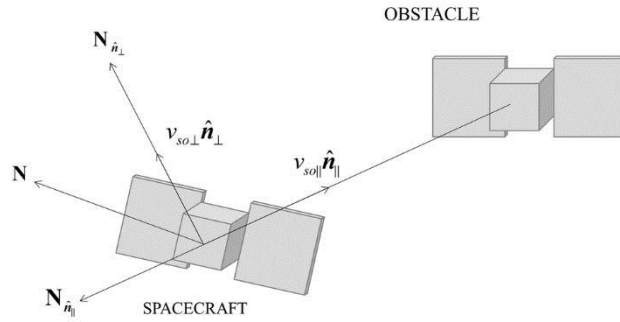

Fig 2: Vector elements of the repelling force

In the forthcoming case studies including multiple spacecraft, one spacecraft sees all other spacecraft as obstacles. Therefore, the total repulsive acceleration for one spacecraft is simply defined as the summation of all the repulsive accelerations due to the rest of the spacecraft in formation

$$\mathbf{N}_{total,k} = \sum_{\substack{i=1 \\ i \neq k}}^{b} \mathbf{N}_i$$

(19)

where k represents the current spacecraft and b the total number of spacecraft involved in the maneuvers. Implementing together the tracking scheme and the collision avoidance system (CAS) results in the control strategy illustrated in Fig. 3.
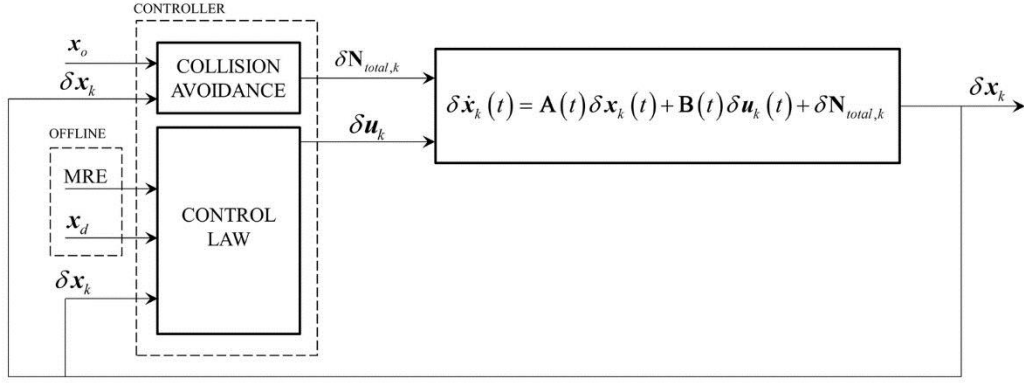
Fig. 3: Guidance and control scheme

4. Case studies

To demonstrate the effectiveness of the proposed guidance and control system, two simulated scenarios are presented in the next subsections using eccentric reference orbits and PRISMA as reference mission. In these scenarios, several followers transfer to and then track a predefined target nominal trajectory while collision between the elements of the formation is avoided. The proposed controller is implemented using the model in Eq. (2) together with the control law in Eq. (7) and the CAS in Eq. (18) and it is assumed that no external perturbations, such as J2 and atmospheric drag, affect the performance of the satellites and the controller. The capabilities of the proposed controller are analyzed in terms of values of total maneuver delta-v (Δv) and fuel consumption, calculated using the equations $\Delta v = \int_{t_0}^{t} \left\| \boldsymbol{u}_T(t) \right\| dt$ and $m_f = m_0 \exp\left(\Delta v / g_0 I_{sp} \right)$ respectively, with and without the effects of the CAS. When considering the effects of the CAS, the vector $\boldsymbol{u}_T$ corresponds to the sum of the control input and the repelling acceleration. The values of m_0 and I_{sp} used in the following scenarios are defined in the next subsection and $g_0 = 9.81$ m/s^2.

4.1 Highlights of the PRISMA mission

PRISMA has the objective of testing spacecraft formation flying capacities for future space missions and it was designed by the Swedish National Space Board and OHB Sweden. Within this project, the German Aerospace Center (DLR) and the German Space Operations Center (GSOC) contribute with the Spaceborne Autonomous Formation Flying Experiment (SAFE), implementing autonomous guidance laws and robust control algorithms for safe separation, formation keeping and reconfiguration of formations in close proximity. The PRISMA mission comprises two satellites, Mango (the follower) and Tango (the leader) in a reference orbit with 750 km of mean altitude, 0.004 of eccentricity and 98.28° of inclination. Relevant physical features of these satellites are summarized in Table 1 (D'Amico et al., 2013). In the following scenarios, it is assumed that Mango thrusters provide continuously-variable low-thrust during the controlled maneuver.

	Mango	Tango
Main Body (mm)	750 x 750 x 820	570 x 740 x 295
Deployed (mm)	2600	N/A
Wet Mass (kg)	150	40
Propulsion (N)	6 x 1 ($I_{sp} = 220s$)	N/A
Cross-section (m^2)	1.3 (or 2.75[a])	0.38
Drag Coefficient	2.5	2.25

[a] After solar panels are deployed

Table 1: Summary of relevant physical features of Mango and Tango

4.2 Scenario 1

This scenario simulates the on-orbit transfer of two Mango satellites with initial and final conditions as indicated in Table 2. The reference orbit has an eccentricity of 0.25, a perigee of 450 km and a period of 2.4 hours. First, the scenario is simulated without the effects of the CAS and its results are compared to those obtained when the CAS is active. In this scenario, the diagonal of the LQR gains are selected to be $\mathbf{Q} = diag\begin{bmatrix} 150 & 150 & 150 \end{bmatrix}$, $\mathbf{R} = diag\begin{bmatrix} 1 & 1 & 1 \end{bmatrix}$ and $\mathbf{F} = diag\begin{bmatrix} 150 & 150 & 150 \end{bmatrix}$. In both scenarios, it is assumed that every Mango occupies a spherical volume with a diameter of 2.6 m, taking into account the fully-deployed solar panels of Mango (See Table 1). However, a virtual safety layer is added to every spacecraft, by means of the parameter D in Eq. (10), surrounding each one of them with a spherical volume of 5 m diameter. The rest of the CAS parameters in Eq. (10) are chosen as $\lambda = 1 \times 10^{-7}$ and $a_d = 0.1$ m/s. Starting at the perigee of the reference orbit, the planar maneuver carried out by both satellites during the simulation with and without the CAS is showed in Fig. 4, in terms of displacement in the *x-y* LVLH plane. It is observed in Fig. 4a that without the effects of the CAS the spacecraft maneuvering generates a collision threat. On the other hand, Fig 4b shows that the trajectory of the two satellites initially approach each other but then they are repelled by the forces generated by the CAS. These avoidance actions are more visible in Fig. 5 where the separation distance between the spacecraft is plotted for the complete maneuvering time. It is also observed in Fig. 5a that without the CAS the spacecraft violate the virtual safety layer generating a collision threat between them. Using the CAS with the previously selected parameters allow these separation distances to be shifted beyond the safety limit, as observed in Fig. 5b, decreasing the collision risk of the maneuver. This shift is also perceived in the error dynamics as indicated in Fig. 6a in contrast with Fig. 6b, where the additional maneuvering to avoid collision can be also observed. This feature is likewise observable in the thrust behavior as seen in Fig. 7 where an additional amount of thrust is required to carry out the avoidance movement. This behavior has an impact on Δv and fuel consumption, as observed in Table 3, where the requirements of the maneuvering to avoid collision creates a difference between the values obtained with and without CAS. For instance, Mango 1 increases its total maneuver Δv and fuel consumption by 40%. Tuning the CAS parameters has implications not only in the performance of the spacecraft but also the final results of total maneuver Δv and fuel consumption, since the contribution of the artificial repelling acceleration is directly related to the calculation of these quantities, as mentioned at the beginning if this section. For example, considering the maneuver and results presented in this scenario, an increase in the value of the parameter D would provide a larger virtual safety volume and also would contribute to increase the magnitude of the repelling acceleration, and therefore Δv and fuel consumption, since D is included twice in the expression of the repelling acceleration in Eq. (18) as an inverse negative exponential. A similar result may be obtained by increasing the CAS parameter λ, which acts as a gain used to tune up the overall magnitude of the repelling acceleration. Moreover, the deceleration parameter a_d also contributes to the overall magnitude of the repelling acceleration. When tuned-up, a_d modifies the value of the virtual distance d_a the maneuvering spacecraft requires to travel in order to decrease the quantity $v_{so\parallel}$ to zero. The larger the value of a_d the largest the values of Δv and fuel consumption. These features are implemented and verified as follows. Simulating Scenario 1 using the same gain matrices and CAS parameters, but changing the value of λ to 1.5×10^{-7}, yields larger Δv and fuel consumption in Mango 2, for instance, with values of 11.82 m/s and 819 g respectively, as shown in Table 4. This table also shows that selecting an effective distance of $D = 7$ m, while leaving the rest of the parameters and gains as previously defined in the scenario, increases Mango 2 Δv and fuel consumption to 1.18 m/s and 82.24 g respectively. Moreover, choosing the CAS parameter a_d to 1 m/s^2 leads to an increase in these values to 5.57 m/s and 386.85 g.

	Mango 1	Mango 2
Initial position (m)	$\begin{bmatrix} -15 & -50 & 0 \end{bmatrix}^T$	$\begin{bmatrix} 15 & -50 & 0 \end{bmatrix}^T$
Initial velocity (m/s)	$\begin{bmatrix} 0.35 & 0.35 & 0 \end{bmatrix}^T$	$\begin{bmatrix} -0.17 & 0.17 & 0 \end{bmatrix}^T$
Final position (m)	$\begin{bmatrix} -15 & 0 & 0 \end{bmatrix}^T$	$\begin{bmatrix} 15 & 0 & 0 \end{bmatrix}^T$
Final velocity (m/s)	$\begin{bmatrix} 0 & 0 & 0 \end{bmatrix}^T$	$\begin{bmatrix} 0 & 0 & 0 \end{bmatrix}^T$

Table 2: Initial and final conditions in Scenario 1

a) Without CAS

b) With CAS
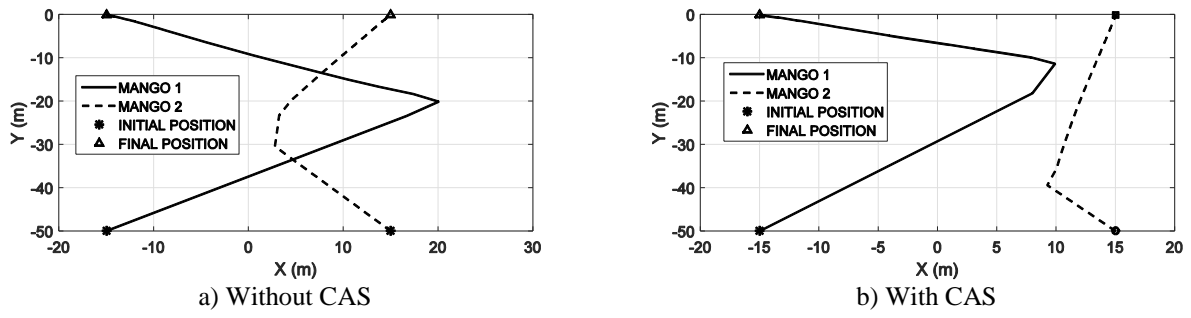
Fig. 4: Maneuver trajectory in Scenario 1

a) Without CAS

b) With CAS
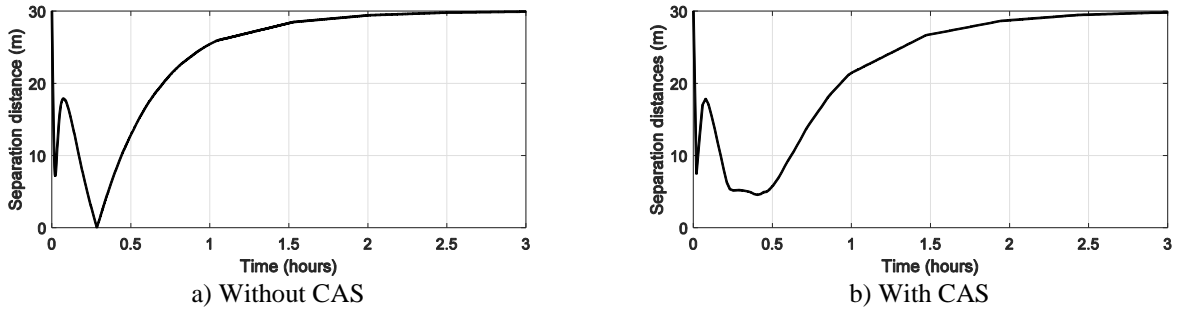
Fig. 5: Separation distance in Scenario 1

a) Without CAS

b) With CAS
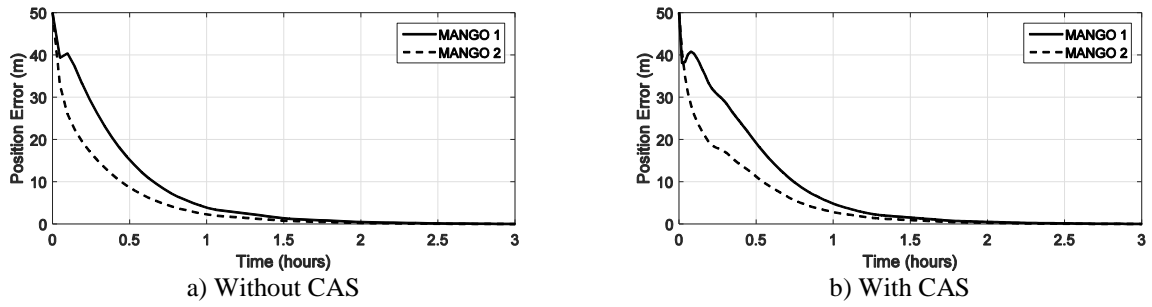
Fig. 6: Magnitude of the position error in Scenario 1

a) Without CAS
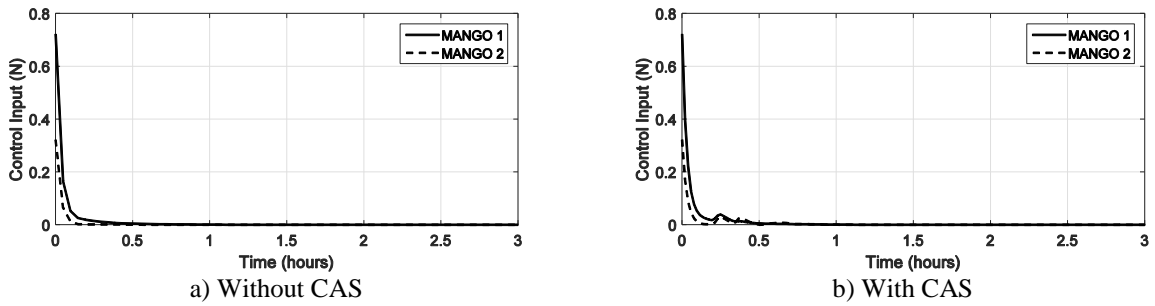
b) With CAS

Fig. 7: Magnitude of the control input in Scenario 1

	MANGO 1	MANGO 2	TOTAL
WITHOUT CAS			
Δv (m/s)	0.72	0.24	0.969
Fuel Consumption (g)	50.12	17.33	67.45
Max. Thrust (N)	0.72	0.32	N/A
Final Position Error (m)	0	0	N/A
Final Velocity Error (m/s)	0	0	N/A
WITH CAS			
Δv (m/s)	1.01	1	2.01
Fuel Consumption (g)	70.65	69.62	140.27
Max. Thrust (N)	0.72	0.322	N/A
Final Position Error (m)	0	0	N/A
Final Velocity Error (m/s)	0	0	N/A

Table 3: Summary of results for Scenario 1

Parameter	Δv (m/s)	Fuel Consumption (g)
$D = 7\ m$	1.18	82.24
$\lambda = 1.5 \times 10^{-7}$	11.82	819.71
$a_d = 1$ m/s^2	5.57	386.85

Table 4: CAS parameters tune-up and corresponding Δv
and fuel consumption for Mango 2. Each row represents a test case where the named parameter is set as specified, while the others are those defined in Scenario 1

4.3 Scenario 2

In this scenario, a maneuver with four Mango satellites is simulated, each located at one vertex of an imaginary square with side length of 20 m in the *y-z* plane and centered at the origin of the LVLH reference frame, with initial and final states as observed in Table 5. The objective of this maneuver is to swap positions diagonally while avoiding collision between the spacecraft. The LQR matrices are chosen with the same values as in the previous scenario and the CAS parameters are selected as $D = 5$ m, $\lambda = 1 \times 10^{-6}$ and $a_d = 15$ m/s^2. The 3D maneuver, with and without the effects of the CAS, is shown in Fig. 8. When a collision avoidance action is taken, extra maneuvering is observed, as in Fig. 8b, in contrast with those maneuvers without CAS in Fig. 8a. These avoidance actions are also visible in Fig. 9 where the separation distance between each spacecraft is plotted for the complete maneuver. In Fig. 9a, it is also observed that without the CAS some spacecraft generate a collision threat, which vanishes when the CAS is activated shifting the separation distances above the safety limit, as observed in Fig. 9b. This shift is also perceived in the error dynamics as indicated in Fig. 10a in contrast with Fig. 10b and in the thrust behavior as seen in Fig. 11a and 11b. As expected, these avoidance maneuvers modify the results in terms of Δv and fuel consumption, as observed in Table 6, where differences are showed between the values obtained with and without CAS; for example, Mango 3 increased its Δv and fuel consumption by approximately 1500%.

	Mango 1	**Tango 2**	**Mango 3**	**Mango 4**
Initial position (m)	$\begin{bmatrix} 0 & -10 & 10 \end{bmatrix}^T$	$\begin{bmatrix} 0 & 10 & 10 \end{bmatrix}^T$	$\begin{bmatrix} 0 & 10 & -10 \end{bmatrix}^T$	$\begin{bmatrix} 0 & -10 & -10 \end{bmatrix}^T$
Initial velocity (m/s)	$\begin{bmatrix} 0 & 0 & 0 \end{bmatrix}^T$	$\begin{bmatrix} 0 & 0 & 0 \end{bmatrix}^T$	$\begin{bmatrix} 0 & 0 & 0 \end{bmatrix}^T$	$\begin{bmatrix} 0 & 0 & 0 \end{bmatrix}^T$
Final position (m)	$\begin{bmatrix} 0 & 10 & -10 \end{bmatrix}^T$	$\begin{bmatrix} 0 & -10 & -10 \end{bmatrix}^T$	$\begin{bmatrix} 0 & -10 & 10 \end{bmatrix}^T$	$\begin{bmatrix} 0 & 10 & 10 \end{bmatrix}^T$
Final velocity (m/s)	$\begin{bmatrix} 0 & 0 & 0 \end{bmatrix}^T$	$\begin{bmatrix} 0 & 0 & 0 \end{bmatrix}^T$	$\begin{bmatrix} 0 & 0 & 0 \end{bmatrix}^T$	$\begin{bmatrix} 0 & 0 & 0 \end{bmatrix}^T$

Table 5: Initial and final conditions in Scenario 2

a) Without CAS b) With CAS
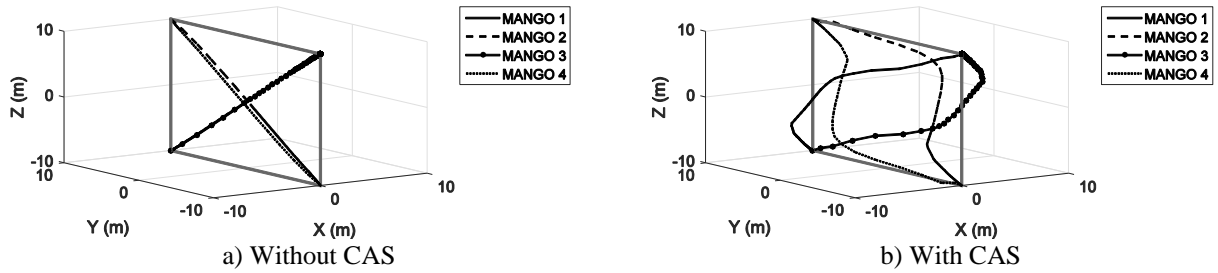
Fig. 8: Maneuver trajectory in Scenario 2

a) Without CAS b) With CAS
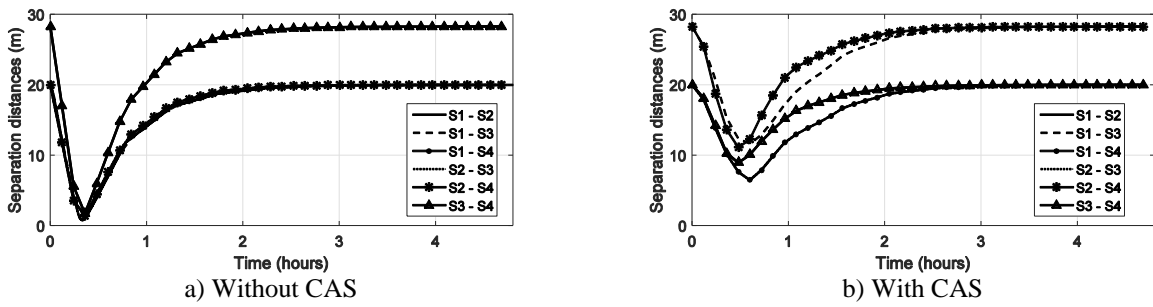
Fig. 9: Separation distance in Scenario 2

a) Without CAS b) With CAS
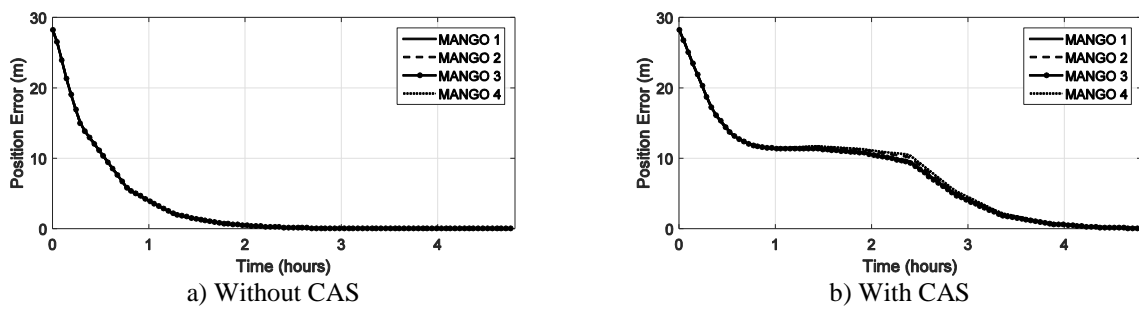
Fig. 10: Magnitude of the position error in Scenario 2

a) Without CAS   b) With CAS
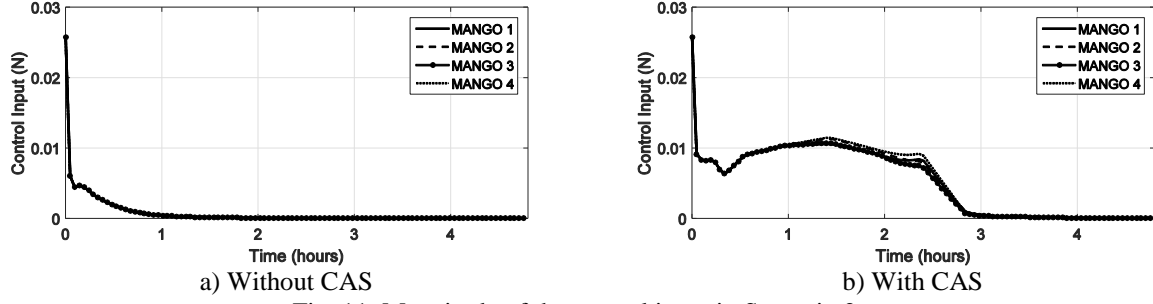
Fig. 11: Magnitude of the control input in Scenario 2

	MANGO 1	MANGO 2	MANGO 3	MANGO 4	TOTAL
WITHOUT CAS					
Δv (m/s)	0.071	0.071	0.071	0.071	0.284
Fuel Consumption (g)	4.94	4.94	4.94	4.94	19.76
Max. Thrust (N)	0.025	0.025	0.025	0.025	N/A
Final Position Error (m)	0.001	0.001	0.001	0.001	N/A
Final Velocity Error (m/s)	0	0	0	0	N/A
WITH CAS					
Δv (m/s)	1.09	1.12	1.09	1.12	4.42
Fuel Consumption (g)	76.32	78.28	76.32	78.28	309.2
Max. Thrust (N)	0.04	0.04	0.04	0.04	N/A
Final Position Error (m)	0.002	0.002	0.002	0.002	N/A
Final Velocity Error (m/s)	0	0	0	0	N/A

Table 6: Summary of results for Scenario 2

5. Conclusions

A tracking controller with collision avoidance capabilities for formation flying in close proximity was presented using Riccati procedure in eccentric reference orbits. The proposed dynamical model incorporates repulsive accelerations from an artificial potential field, in order to perform collision avoidance during proximity operations. The controller was implemented in two scenarios for spacecraft formation reconfiguration and swapping. These scenarios showed that the performance of the controllers, in terms of total maneuver Δv and fuel consumption, was affected by the selection of the CAS parameters. In both scenarios several spacecraft were simulated with the proposed controller and its performance was compared with and without the influence of the CAS. Both cases showed that the controller allowed the spacecraft to effectively track the nominal trajectory with a final error close to zero. The simulations including CAS showed an effective decrease of collision risk during the performance of the maneuver. The same simulations also showed increments in total Δv and fuel consumption with respect to the same maneuver without CAS, although this increment was expected, since the spacecraft required additional collision avoidance maneuvers, especially in those spacecraft with higher collision risk. Further studies will be done to determine the optimal values of the CAS parameters. For future work, we will add scenarios with long-time horizons to test the controller performance along with perturbations like J2 and atmospheric drag.

References

Badawy, A. & McInnes, C., 2008. On-Orbit Assembly Using Superquadric Potential Fields. *Journal of Guidance Control and Dynamics*, 31(1), pp.30–43.

Bainum, P.M. et al., 2005. Techniques for deploying elliptically orbiting constellations in along-track formation. *Acta Astronautica*, 57(9), pp.685–697.

Bate, R., Mueller, D. & White, J., 1971. *Fundamentals of Astrodynamics*, New York: Dover Publications Inc.

Bennet, D. & McInnes, C.., 2008. Pattern transition in spacecraft formation flying via the artificial potential field method and bifurcation theory. *3rd International Symposium on Formation Flying, Missions and Technologies*.

Bryson, A.E. & Ho, Y.-C., 1975. *Applied Optimal Control: Optimization, Estimation, and Control*, Taylor & Francis.

Capo-Lugo, P.A. & Bainum, P.M., 2007. Active Control Schemes Based on the Linearized Tschauner–Hempel Equations to Maintain the Separation Distance Constraints for the NASA Benchmark Tetrahedron Constellation. *Journal of Mechanics of Materials and Structures*, 2(8).

Clohessy, W. & Wiltshire, R., 1960. Terminal Guidance System for Satellite Rendezvous. *Journal of the Astronautical Sciences*, 27(9), pp.653–678.

D'Amico, S., Ardaens, J.-S. & De Florio, S., 2013. Autonomous formation flying based on GPS — PRISMA flight results. *Acta Astronautica*, 82(1), pp.69–79.

De Florio, S., D'Amico, S. & Radice, G., 2014. Virtual Formation Method for Precise Autonomous Absolute Orbit Control. *Journal of Guidance, Control, and Dynamics*, 37(2), pp.425–438.

Ge, S. & Cui, Y., 2002. Dynamic motion planning for mobile robots using potential field method. *Autonomous Robots*, 13, pp.207–222.

Gurfil, P., 2005. Relative motion between elliptic orbits: generalized boundedness conditions and optimal formationkeeping. *Journal of Guidance, Control, and Dynamics*.

Huang, X., Yan, Y. & Zhou, Y., 2014. Optimal spacecraft formation establishment and reconfiguration propelled by the geomagnetic Lorentz force. *Advances in Space Research*, 54(11), pp.2318–2335.

Inalhan, G., Tillerson, M. & How, J.P., 2002. Relative dynamics and control of spacecraft formations in eccentric orbits. *Journal of Guidance Control and Dynamics*, 25(1), pp.48–59.

Lamy, A., Julien, E. & Flamenbaum, D., 2009. Four Year Experience of Operational Implementation of Autonomous Orbit Control: Lessons Learned, Feedback and Perspectives. *... of the 21st International Symposium on ...*.

Lee, D., Sanyal, A.K. & Butcher, E. a., 2015. Asymptotic Tracking Control for Spacecraft Formation Flying with Decentralized Collision Avoidance. *Journal of Guidance, Control, and Dynamics*, 38(4), pp.587–600. Available at: http://arc.aiaa.org/doi/10.2514/1.G000101.

McCamish, S.B., Romano, M. & Yun, X., 2007. Autonomous Distributed Control Algorithm for Multiple Spacecraft in Close Proximity Operation. In *AIAA Guidance, Navigation and Control Conference and Exhibit*.

McInnes, C.R., 1993. Autonomous Proximity Maneuvering Using Artificial Potential Functions. *European Space Agency Journal*, 17(2), pp.159–169.

McQuade, F. & McInnes, C.R., 1997. Autonomous control for on-orbit assembly using potential function methods. *Aeronautical Journal*, 101(1006), pp.255–262.

Montenbruck, O. & Kahle, R., 2008. Navigation and control of the TanDEM-X formation. *The Journal of the Astronautical Sciences*, 56(3), pp.341–357.

Palmer, P., 2006. Optimal Relocation of Satellites Flying in Near-Circular-Orbit Formations. *Journal of Guidance, Control, and Dynamics*, 29(3), pp.519–526.

Plam, Y. et al., 2008. Autonomous Orbit Control Experience on TacSat-2 using Microcosm's Orbit Control Kit (OCK). *31st Annual AAS Guidance and Control Conference*.

Starin, S., 2001. Design of a LQR controller of reduced inputs for multiple spacecraft formation flying. *American Control Conference*, 2, pp.1327–1332.

Tschauner, J.F.A. & Hempel, P.R., 1965. Rendezvous zu einemin Elliptischer Bahn umlaufenden Ziel. *Acta Astronautica*, 11(2), pp.104–109.

Yoo, S. et al., 2013. Spacecraft fuel-optimal and balancing maneuvers for a class of formation reconfiguration problems. *Advances in Space Research*, 52(8), pp.1476–1488.